Reasonable suppression of polysulfides/polyselenides shuttle based on MXene in Na-SeS_2 batteries

Qiu-Ju Yang, Jing Zhao, Wei Gao, Wei Zhong, Yu-Ruo Qi*, Jin Han, Shu-Juan Bao, Mao-Wen Xu*

Abstract Metal-sulfur/selenium batteries have become the focus of new-generation energy storage systems due to the advantages of low-cost and high energy density. However, it still suffers from the notorious shuttle of polysulfides/polyselenides, poor electronic conductivity and tremendous volume expansion. Herein, a dual defense system for polysulfides/polyselenides was proposed and constructed based on MXene. The nitrogen-doped porous carbon (NPC) decorated by $Ti_3C_2T_x$ MXene (M@NPC) was employed as the SeS_2 host (SeS_2@M@NPC). Particularly, $Ti_3C_2T_x$ sheets wrapped on NPC guarantee the rapid ion diffusion and serve as the first barrier for SeS_2 and dissolved sodium polysulfides/polyselenides. Meanwhile, the few-layered $Ti_3C_2T_x$ sheets coated on glass fiber separators act as the second barrier for alleviating the shuttle of polysulfides/polyselenides through physical interception and chemical adsorption. With this elaborate design, the integrated Na-SeS_2 battery achieves a high specific capacity of 1243 mAh·g^{-1} at 1.0C, revealing a distinct superiority over its counterparts (SeS_2@M@NPC, 1083 mAh·g^{-1} at 0.5C; and SeS_2@NPC, 823 mAh·g^{-1} at 0.5C). The findings gained in this work provide a creative idea for the construction of durable room-temperature Na-SeS_2 batteries based on MXenes and their derivative materials.

Keywords MXene; Integrated strategy; Shuttle effect; Room temperature (RT) Na-SeS_2 batteries

1 Introduction

Lithium-ion batteries (LIBs) that commonly used in portable electronic equipment are unable to meet the requirements of grid-scale energy storage systems and long-range electric vehicles. Under this occasion, room temperature sodium-sulfur (room temperature (RT) Na-S) batteries whose theoretical specific capacity and energy density far surpass those of LIBs have aroused extensive interests from scientific researchers [1, 2]. Sodium compounds are more thermodynamically stable than lithium, which are considered to be advantageous features when designing batteries. Moreover, sodium and sulfur possess additional advantages of non-toxicity, resource-rich and low-cost [3, 4]. Therefore, it is imperative to develop RT Na-S batteries.

However, RT Na-S batteries suffer from the sluggish electrochemical reaction kinetics, because the solid sulfur is insulated and displays a low reactivity with sodium. Moreover, the solid sulfur would undergo tremendous volume expansion during charge/discharge. Worst of all, the notorious shuttle effect of polysulfides leads to serious loss of active materials, thereby fading the capacity [5]. Accordingly, some progress has been made by researchers to alleviate these troublesome issues. For instance, a

Q.-J. Yang, J. Zhao, W. Gao, W. Zhong, Y.-R. Qi*, S.-J. Bao, M.-W. Xu*
School of Materials and Energy, Southwest University, Chongqing 400715, China
e-mail: qiyuruojy@swu.edu.cn

M.-W. Xu
e-mail: xumaowen@swu.edu.cn

J. Han
Helmholtz Institute Ulm, Ulm 89081, Germany

J. Han
Karlsruhe Institute of Technology, Karlsruhe 76021, Germany

railway-like network electrode was designed for developing Na-S battery by Yang et al. [6] and a dual-porosity carbon matrix was prepared by Liu et al. [7] as sulfur host.

In particular, Selenium-sulfur solid solutions (Se_xS_y) are capable to address the above problems. Se_xS_y is a kind of cathode materials with varied proportions of Se-S, combining the high conductivity of Se with the high specific capacity of S, which possess improved electronic conductivity and enhanced reaction kinetics [8]. SeS_2 was widely employed in Li-SeS_2 and Na-SeS_2 batteries, since the first report from Amine's group in 2012 [9–12]. Despite this, the shuttle of soluble long-chain sodium polysulfides/polyselenides (Na_2S_x, Na_2Se_x, $4 \leq x \leq 8$) continues to be a challenge for this battery system. As shown in Fig. 1a, in common configuration, the diffusion of soluble long-chain sodium polysulfides/polyselenides would inevitably lead to loss of active materials and unwanted redox reactions on the surface of metallic sodium.

Owing to the high electronic conductivity and abundant active sites, MXene has been developed continuously with a focus on energy storage, electromagnetic interference shielding, environmental, sensor and biomedical fields since it was first discovered in 2011. Furthermore, it has been reported that MXene can help promote the chemisorption of polysulfides through forming Ti–S bonds via Lewis acid–base interaction, a favorable feature for improving electrochemical performances of Li/Na-S batteries [13, 14]. For example, Wu and co-workers reported an all-MXene-based integrated electrode to enable high-performance Li–S batteries [15].

However, even though some strategies were adopted in cathode, a few escaped polysulfides/polyselenides still step over the separator and enter the anode area during cycling. More importantly, the safety of Na-SeS_2 battery will be threatened with the formation of sodium dendrites and undesirable reactions between Na and polysulfides/polyselenides [16]. Therefore, according to the configuration of the Na-SeS_2 battery, it is a feasible strategy to design an intermediate layer on the separator of cathode-side as effective barrier and reservoir for polysilfides/polyselenides.

Herein, we designed a dual defense system based on MXene to inhibit the shuttle of polysulfides/polyselenides in Na-SeS_2 batteries. Firstly, nitrogen-doped porous carbon (NPC) derived from zeolitic imidazolate framework (ZIF)-8 provides the storage space for SeS_2, while $Ti_3C_2T_x$-MXene decorated on the surface of NPC enhance the conductivity of the cathode and thus guarantee rapid ion diffusion. This hierarchical composite (M@NPC) serves as the-first-barrier to retard the dissolution of SeS_2 and the shuttle of dissolved sodium polysulfides/polyselenides. Additionally, the few-layered $Ti_3C_2T_x$ sheets were uniformly scattered on the separator to act as interlayer, which is the second helper for preventing the shuttle of overflowed polysulfides/polyselenides, as illustrated in Fig. 1b. Consequently, the dual defense system can effectively resist the shuttle of polysulfides/polyselenides and the Na-SeS_2 battery delivers a high specific capacity and remarkable rate capability.

2 Experimental

2.1 Synthesis

2.1.1 Synthesis of nitrogen-doped porous carbon derived from ZIF-8 (NPC)

In a typical procedure, 0.72 g $Zn(NO_3)_2{\cdot}6H_2O$ was dissolved in deionized water with magnetically stirring as uniform Solution A. Meanwhile, 10.8 g 2-methylimidazole was added into 100 ml deionized water and ultrasonically

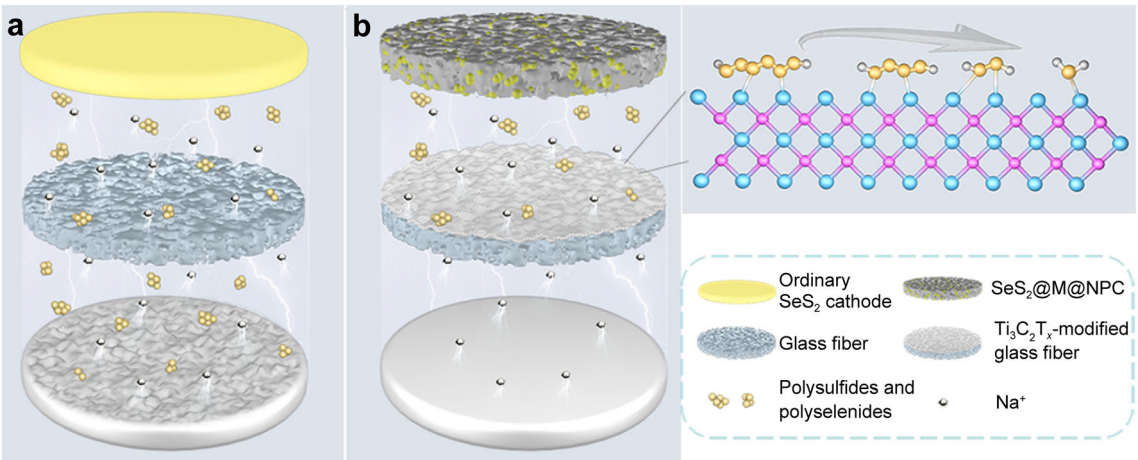

Fig. 1 Schematic diagrams of **a** a common Na-SeS_2 battery and **b** a Na-SeS_2 battery based on SeS_2@M@NPC cathode and $Ti_3C_2T_x$-modified glass fiber separator

dispersed for 10 min as Solution B. After adding Solution A into Solution B, the mixture was aged for 12 h at room temperature. Finally, the white precipitate was collected by centrifuging and thoroughly rinsed with deionized water and ethanol several times. After drying at 60 °C overnight, the as-synthesized product was treated at 800 °C for 2 h with a ramp rate of 2 °C·min^{-1} in Ar atmosphere. After carbonization, the black powder was soaked in hydrochloric acid (HCl) solution (6 mol·L^{-1}) to remove the remaining zinc. The NPC was obtained by vacuum filtration and thoroughly washed with deionized water, and dried at 60 °C for 12 h.

2.1.2 Synthesis of few-layer MXene-$Ti_3C_2T_x$ sheets

The few-layer sheets were prepared by etching Ti_3AlC_2 with HCl and LiF. In detail, 1 g LiF was dissolved in 20 ml HCl solution. When it was completely dissolved, 1 g Ti_3AlC_2 was soaked in the above solution and kept at 35 °C for 24 h. Subsequently, centrifuging the suspension until the pH reached ~ 7. Then, the precipitate was dispersed into 200 ml deionized water and ultrasonic treated for 3 h. Whereafter, the solution was centrifuged with 3500 r·min^{-1} for 30 min to obtain the few-layered $Ti_3C_2T_x$ sheets, which was stored in the refrigerator for further use.

2.1.3 Synthesis of nitrogen-doped porous carbon coated with MXene (M@NPC)

Typically, 40 mg NPC was dispersed with ultrasonic in 200 ml deionized water. Meanwhile, the prepared $Ti_3C_2T_x$ solution was diluted to 1 mg·ml^{-1}. After 20 min, the above two solutions were mixed and stirred at room temperature for 24 h, filtered and dried to obtain M@NPC.

2.1.4 Synthesis of SeS_2@M@NPC

M@NPC and SeS_2 were mixed and ground in a weight ratio of 2:3. The mixture was then placed in a ceramic boat and annealed at 180 °C for 12 h in a tube furnace to acquire the final SeS_2@M@NPC. The SeS_2@NPC could also be obtained by the same process.

2.1.5 Synthesis of Na_2S_4/Na_2Se_4

The Na_2S and SeS_2 powders were added to 10 ml 1,3-dioxolane (DOL) and diethylene glycol dimethyl ether (DIGLYME) mixed solvent (1:1 vol%) with a molar ratio of 1:1. Then, it was stirred at 60 °C for 8 h to obtain 0.5 mmol·L^{-1} Na_2S_4/Na_2Se_4 mixed solution.

2.2 Characterization

The morphology was explored by field emission scanning electron microscopy (FESEM, JSM-7800F, Japan) and transmission electron microscopy (TEM, JEM-2100, Japan). Composition of the products was analyzed by energy dispersive spectroscopy (EDS, JEOL-6300F). The crystal structures were recorded through X-ray diffraction (XRD, MAXima-X XRD-7000, Cu Kα radiation, λ = 0.15416 nm). HR Evolution (Horiba) with 532 nm laser was used to collect Raman spectrum. In-situ Raman spectrum was recorded by jointing EL-CELL (Germany) and electrochemical workstation. The specific surface area and pore volume were measured by Brunauer–Emmett–Teller method (BET, Quadrasorb Evo 2QDS-MP-30). The sulfur content was acquired from thermo-gravimetric analysis (TGA, Q50, USA) under nitrogen atmosphere. The elemental composition of the material was tested by X-ray photoelectron spectroscopy (XPS, ESCALAB 250Xi electron spectrometer, Thermo Scientific). The charge of materials was measured by the Zeta potential instrument (Zetasizer Nano ZS90, Malvern).

2.3 Electrochemical measurements

CR 2032 cells were assembled to test electrochemical performance. The working electrodes were fabricated by slurry coating method, which was made by mixing 70 wt% SeS_2@M@NPC, 20 wt% of acetylene black (AB) and 10 wt% of polyvinylidene difluoride (PVDF) in N-methylpyrrolidone (NMP). After mixing uniformly, the slurry was pasted on the aluminum foil and then dried in vacuum at 60 °C overnight. The loading of SeS_2 on each electrode was around 0.5 mg·cm^{-2}. The sodium metal was used as the counter electrode. The separators were glass fiber membranes (Whatman GF/A) coated with that of $Ti_3C_2T_x$ sheets, which were obtained by coating the slurry of 80 wt% of $Ti_3C_2T_x$ and 20 wt% of PVDF followed by drying at 120 °C under vacuum for 12 h. The electrolyte used was 1.0 $NaPF_6$ dissolved in DOL and DIGLYME (1:1 vol%). All specific capacity calculations were based on the mass of SeS_2 (1.0C refers to a current density of 1345 mA·g^{-1}). The cells were cycled at various current densities between 0.5 and 2.8 V on a Land battery test system (CT2001A, Wuhan Kingnuo Electronic Co., China). Cyclic voltammetry (CV) curves were recorded by CHI 760E (Shanghai Chenhua, China) with a scan rate of 0.1 mV·s^{-1}. Electrochemical impedance spectroscopy (EIS) test was performed by Zahner electrochemical workstation.

3 Results and discussion

A schematic preparation of the hierarchical SeS_2@M@NPC composite is illustrated in Fig. S1. First, NPC was synthesized using zinc nitrate hexahydrate and 2-methylimidazole followed by a high-temperature carbonization at 800 °C and soaking with hydrochloric acid. The NPC inherits the dodecahedron morphology of the precursor and possesses an average particle size of ~ 1.1 μm (Fig. S2). At the same time, few-layered $Ti_3C_2T_x$ sheets were obtained by etching the MAX phase with LiF and HF according to the previous work [17]. As displayed in Fig. 2a–c and Fig. S3a–c, the delaminated $Ti_3C_2T_x$ sheets present as light-weight and transparent flakes with an impurity-free surface. The XRD pattern in Fig. S3d is highly consistent with the reported literatures [18, 19].

Owing to the hydrophilic functional groups (–OH, –O, –F, etc.) on the surface of $Ti_3C_2T_x$, the zeta potential of $Ti_3C_2T_x$ was negative, while the zeta potential of NPC was detected to be positive (Fig. S4). Therefore, the M@NPC composite (NPC wrapped with MXene) was successfully prepared via the electrostatic self-assembly between the negative-charged $Ti_3C_2T_x$ and positive-charged NPC.

FESEM and TEM images of the as-prepared M@NPC were displayed in Fig. 2d–f. The NPC polyhedras are tightly embedded in and are perfectly connected by these conductive $Ti_3C_2T_x$ sheets. Figure 2j shows the XRD pattern of M@NPC, as compared with that of $Ti_3C_2T_x$-MXene. The peak at a 2θ degree of 6° corresponds to the (002) plane of $Ti_3C_2T_x$ and the peak around 24.3° is originated from the amorphous carbon in NPC (the XRD pattern of NPC was shown in Fig. S5). In addition, M@NPC exhibits similar characteristic Raman peaks with pure $Ti_3C_2T_x$ (Fig. 2k). The XRD pattern (Fig. 2j) and Raman spectrum (Fig. 2k) both indicate the successful preparation of M@NPC. The as-prepared composite possesses a specific surface area of 50.8 $m^2 \cdot g^{-1}$ and pore volume of 0.18 $cm^3 \cdot g^{-1}$ (Fig. 2l).

The hierarchical structure comprising MXene and NPC not only reduces the volume strain of SeS_2 but also can improve the conductivity of SeS_2, which is beneficial to increase the transportation of ions and electrons during cycling, thus maximizing the utilization of active materials. It is the first defense barrier to prevent the overflow of sodium polysulfides/polyselenides (NaPSs and NaPSes).

Besides, the delaminated $Ti_3C_2T_x$ sheets were also coated on the glass fiber separators to further restrain NaPSs/NaPSes, forming the second defense barrier. Figure 2g and inset are the FESEM and corresponding optical photographs of the bare glass fiber separator. The commercial glass fiber separator shows a loose and porous

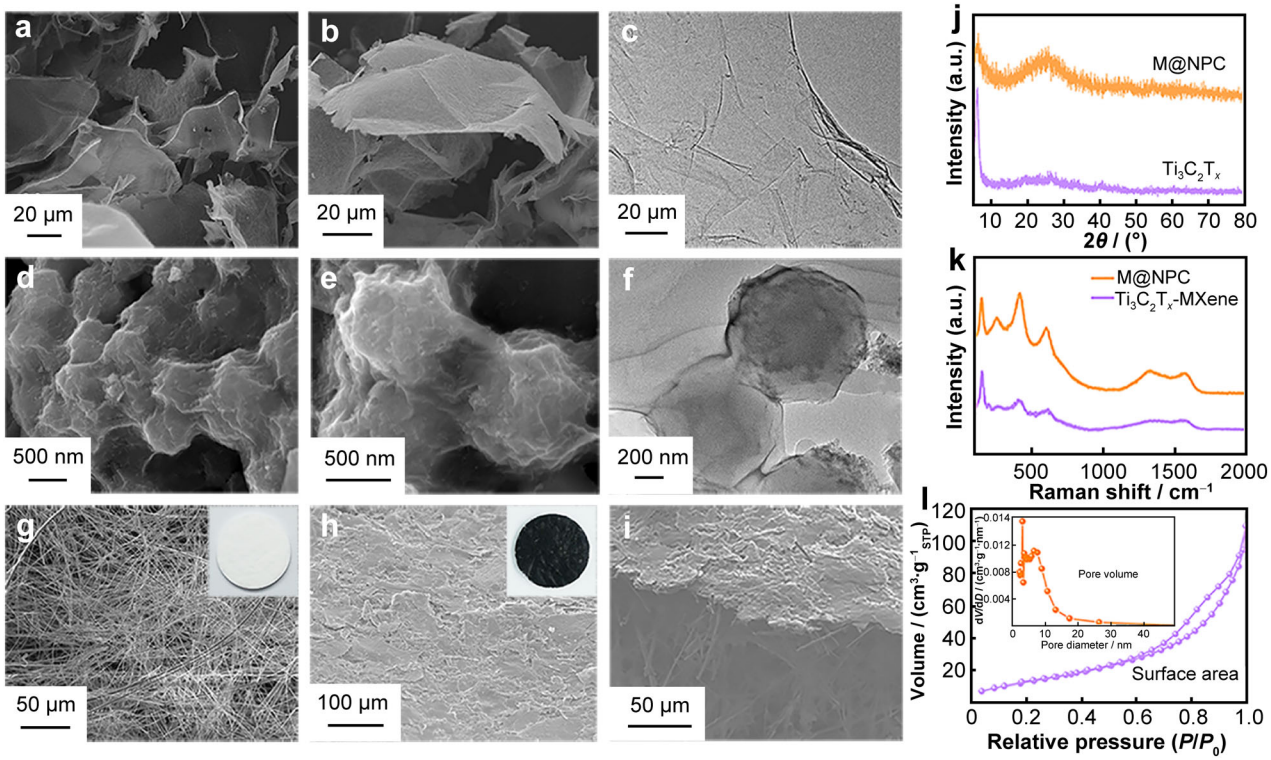

Fig. 2 **a**, **b** FESEM and **c** TEM images of $Ti_3C_2T_x$ sheets; **d, e** FESEM and **f** TEM images of M@NPC; **g, h** FESEM images of glass fiber separator without and with $Ti_3C_2T_x$ sheets coating (insets being corresponding optical photographs); **i** cross-sectional FESEM image of glass fiber separator with coating; **j** XRD patterns and **k** Raman spectra of M@NPC composite and $Ti_3C_2T_x$; **l** BET adsorption/desorption curves of M@NPC and inset being pore-size distribution curve

structure with pore diameters up to several microns, which is easy for NaPSs/NaPSes to pass through. The FESEM images after coating $Ti_3C_2T_x$ sheets are presented in Fig. 2h, i and Fig. S6. It is obvious that the holes are completely covered by $Ti_3C_2T_x$ sheets. The cross-sectional image reveals that the thickness of the intermediate layer is about 10 μm.

The SeS_2@M@NPC electrode was finalized by the infiltration of SeS_2 into the interstice of M@NPC through a melting-diffusion method. According to the TGA curve in Fig. 3a, the SeS_2 content in the M@NPC composite is about 53 wt%, outperforming that in most studies (Fig. S7). The XRD pattern of SeS_2@M@NPC in Fig. 3b shows no obvious signal compared to pure SeS_2, which may be due to the fact that SeS_2 is located in the interior of the M@NPC composite. However, the chemical bonding information of SeS_2 in this composite is successfully detected by XPS. For example, in the high-resolution Se 3d spectrum (Fig. 3c), two pairs of peaks at ~ 55.1/56.2 and ~ 55.7/56.5 eV correspond to the Se–Se homopolar bonds and the Se–S heteropolar bonds, separately. Furthermore, the high-resolution S 2p/Se 3p spectra in Fig. 3d show three pairs of peaks located at 164.9/163.5, 167.6/161.5 and 164.9/162.4 eV, which are assigned to S–S, Se–Se and S–Se bonds respectively [20, 21]. In addition, the specific surface area and pore volume of SeS_2@M@NPC

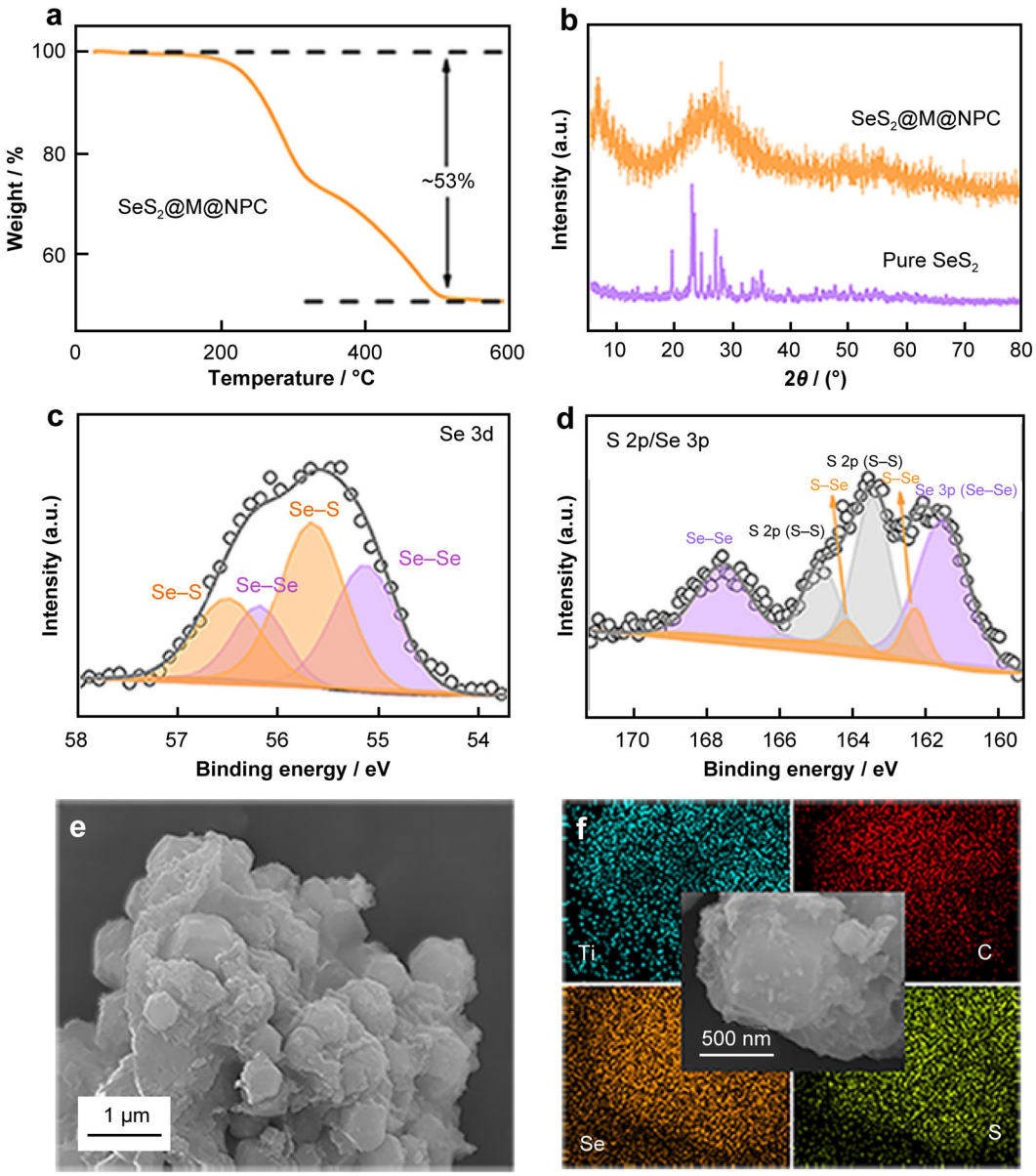

Fig. 3 **a** TGA curve of SeS_2@M@NPC; **b** XRD pattern of SeS_2@M@NPC; high-resolution XPS spectra of **c** Se 3d and **d** S 2p/Se 3p; **e** FESEM image and **f** EDS elemental mapping images of SeS_2@M@NPC

significantly decrease to 8.83 $m^2 \cdot g^{-1}$ and 0.03 $cm^3 \cdot g^{-1}$ (Fig. S8). The remanent pores can suppress the volume expansion of SeS_2 during cycles. Through these analyses, it is found that SeS_2 is successfully diffused into the M@NPC hierarchical structure. Figure 3e demonstrates that the morphology of SeS_2@M@NPC remains intact after sulfur infiltration. The uniform distribution of Ti, C, Se and S elements in the SeS_2@M@NPC hybrid can also be observed by the EDS mapping images in Fig. 3f.

Next, we conducted a pilot study on the electrochemical performances and reaction mechanism of the SeS_2@M@NPC cathode. The room temperature Na-SeS_2 battery was assembled with SeS_2@M@NPC as the cathode and $Ti_3C_2T_x$-modified glass fiber as the separator ($Ti_3C_2T_x$//SeS_2@M@NPC). Figure 4a is the comparison of charge/discharge curves among $Ti_3C_2T_x$//SeS_2@M@NPC, SeS_2@M@NPC and SeS_2@NPC at a current rate of 0.5C. The $Ti_3C_2T_x$//SeS_2@M@NPC battery delivers the smallest polarization and the highest discharge specific capacity of 1210 $mAh \cdot g^{-1}$. It is worth noting that the capacity contribution of M@NPC is negligible under the same conditions (Fig. S9).

The extraordinary superiority of the $Ti_3C_2T_x$//SeS_2@M@NPC electrode is further demonstrated by the excellent rate capability, as shown in Fig. 4b. At various current rates of 0.1C, 0.2C, 0.3C, 0.5C and 1.0C, discharge capacities of 1092, 611, 573, 529 and 479 $mAh \cdot g^{-1}$ are obtained, respectively. Notably, when the current rate goes back to 0.1C, the capacity can return to the original value. In contrast, capacities of SeS_2@M@NPC and SeS_2@NPC decrease almost to 0 $mAh \cdot g^{-1}$ at 1.0C, proving the synergistic effect of the engineered SeS_2@M@NPC electrode and the $Ti_3C_2T_x$-modified separator. The well-reserved voltage plateaus at high current rates (Fig. 4c) further manifest the kinetics advantage of the integrated $Ti_3C_2T_x$//SeS_2@M@NPC battery.

Another appealing property of $Ti_3C_2T_x$//SeS_2@M@NPC is the outstanding cycling performance (Fig. 4d). Remarkably, the $Ti_3C_2T_x$//SeS_2@M@NPC integrated battery delivers a discharge capacity of 1243

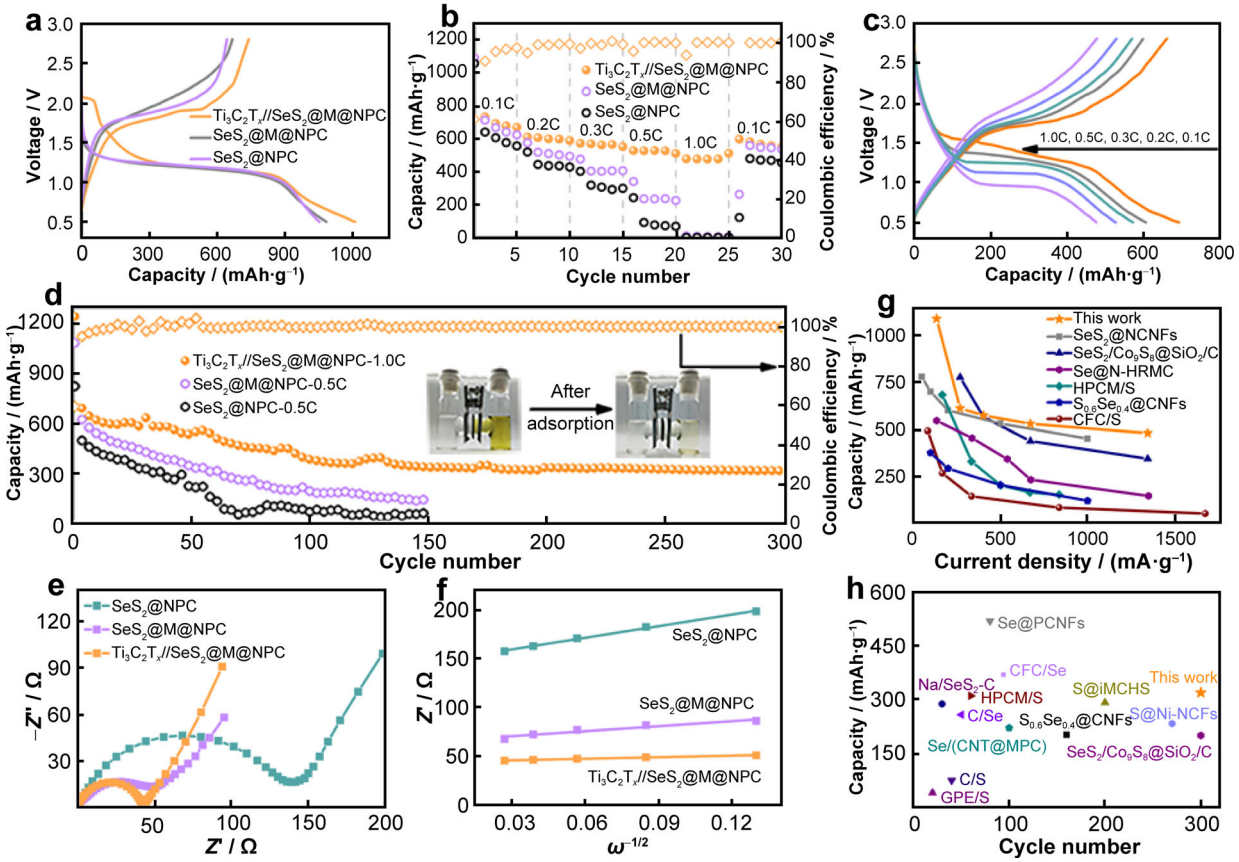

Fig. 4 a Voltage-capacity profiles at 0.5C; **b** rate performances of integrated $Ti_3C_2T_x$//SeS_2@M@NPC, SeS_2@M@NPC and SeS_2@NPC cathodes; **c** voltage-capacity curves at different current rates; **d** cycling performances of integrated $Ti_3C_2T_x$//SeS_2@M@NPC at 1.0C, SeS_2@M@NPC and SeS_2@NPC at 0.5C (inset being adsorption experiment of modified glass fiber membrane to NaPSs/NaPSes); **e** Nyquist plots at open circuit potential before initial discharge; **f** corresponding plots of Z' and $\omega^{-1/2}$ in low frequency of $Ti_3C_2T_x$//SeS_2@M@NPC, SeS_2@M@NPC and SeS_2@NPC; **g** comparison of rate and **h** cycling performance between previous literatures [8, 24–28] and this work

mAh·g^{-1} at 1.0C after 300 cycles with a low capacity decay rate of 0.25% per cycle. In contrast, the SeS_2@M@NPC with the original glass fiber separator displays a decay rate of 0.82% per cycle in 150 cycles and the SeS_2@NPC (SeS_2 loading of ~ 45%, Fig. S10) has a decay rate of 0.92% per cycle in 150 cycles. It is concluded that the MXene coating layer can reduce the volume expansion of SeS_2 and alleviate the shuttle of NaPSs/NaPSes. When further used as an intermediate layer, $Ti_3C_2T_x$ can adsorb the overflowed NaPSs/NaPSes, as demonstrated by adsorption test in inset of Fig. 4d.

Furthermore, the kinetics difference among three cells was probed. Figure 4e compares the electrochemical impedance spectra (EIS) of these three batteries at open circuit potential. The semicircle at high-frequency region belongs to the charge transfer impedance (R_{ct}) while the oblique line at low-frequency area is related to the ion diffusion impedance (Warburg impedance, Z_w) [22, 23]. The R_{ct} of $Ti_3C_2T_x$//SeS_2@M@NPC (42 Ω) is obviously lower than that of SeS_2@M@NPC (49 Ω) and SeS_2@NPC (139 Ω). The fitted linear curve of $Ti_3C_2T_x$//SeS_2@M@NPC between Z' (imaginary part) and $\omega^{-1/2}$ (frequency) (Fig. 4f) displays the smallest slopes, which indicates the greatest Na^+ diffusion coefficient (D_{Na^+}) according to the following formulas:

$$D_{Na^+} = \frac{R^2T^2}{2n^4F^4\delta_w^2A^2C^2} \quad (1)$$

$$Z' = R' + \delta_w\,\omega^{-\frac{1}{2}} \quad (2)$$

where R, T, n, F, A and C are on behalf of gas constant, absolute temperature, number of electrons per molecule during reaction, Faraday's constant, surface area of the work electrode, and Na^+ concentration, respectively. δ_w is the slope of fitted results of Z_w. Accordingly, the Na^+ diffusion coefficients are calculated to be 3.74×10^{-12}, 3.64×10^{-13} and 6.79×10^{-14} cm^2·s^{-1} for $Ti_3C_2T_x$//SeS_2@M@NPC, SeS_2@M@NPC and SeS_2@NPC, respectively. The above results are highly consistent with the rate performance, indicating a rapid charge and mass transfer process for $Ti_3C_2T_x$//SeS_2@M@NPC. As compared with some reported results [8, 24–28], the integrated $Ti_3C_2T_x$//SeS_2@M@NPC battery demonstrates outstanding rate capability and cycle performance (Fig. 4g, h), which illustrates the pivotal advantages in reducing the internal resistance and preventing the shuttle effect.

The reaction mechanism during cycling was explored by CV, ex-situ XRD and in-situ Raman spectra. Figure 5a is the first CV curve in a voltage range of 0.5–2.8 V at a scan rate of 0.1 mV·s^{-1}. In the cathodic scanning, there are two characteristic peaks at 2.06 and 1.14 V, which indicates the transformation of SeS_2 is a multi-step reaction with the formation of intermediates. The peak at 2.06 V is assigned to the reduction of SeS_2 to long-chain sodium polysulfides/polyselenides, while the peak located at 1.14 V is ascribed to the generation of short-chain Na_2S_2/Na_2Se_2 and Na_2S/Na_2Se. In the subsequent anodic process, the peaks around 1.8 and 2.5 V are the oxidation of Na_2S to long-chain sodium polysulfides/polyselenides and subsequently the generation of elemental substances [29, 30].

Furthermore, ex-situ XRD was conducted to determine the phase transition of the SeS_2@M@NPC electrode. As shown in Fig. 5b, no obvious characteristic peak of SeS_2 is detectable at open circuit potential, which may be due to the fact that SeS_2 is located inside the material. It should be noted that peaks at ~ 11° and ~ 15.5° are characteristic peaks of $Ti_3C_2T_x$, while the strong peak at around 44° is derived from the Al foil. At 1.4 V, two peaks of Na_2S_x (Na_2S_5: JCPDS No. 44-0823, Na_2S_3: JCPDS No. 44-0822) arise at 18° and 20°. When further discharged to 1.1 V, an additional Na_2Se peak is also observed at 37.9° (JCPDS No. 23-0527) besides peaks of Na_2S_5 and Na_2S_3. Finally, Na_2S (the peak located at 23.7°, JCPDS No. 47-1698) appears at 0.5 V. During the subsequent charging process, the short-chain polysulfides/polyselenides continuously convert to long-chain Na_2S_x, Na_2Se_x, Se_8 (JCPDS No. 54-0500) and S_8 (JCPDS No. 53-1109).

The above results are also supported by in-situ Raman spectra. As can be seen from Fig. 5c, characteristic peaks of SeS_2 are detected at 237 and 461 cm^{-1} at open circuit potential. When discharging to 1.7 V, long-chain Na_2S_x appears at around 256 cm^{-1}. At 1.5 V, the peak at ~ 355 cm^{-1} indicates the formation of Na_2Se_x [24, 31, 32]. When the discharge process continues, a peak of Na_2S appears at 181.8 cm^{-1} (0.6 V) and a peak of Na_2Se appears at around 225 cm^{-1} (0.5 V). Similarly, in the following charge process to 2.8 V, long-chain sodium polysulfides/polyselenides S_8 and Se_8 are detected gradually.

Additionally, the visible adsorption (Fig. S11a) and ultraviolet–visible (UV–Vis, Fig. S11b) tests were conducted to confirm the adsorption capability of M@NPC. The solution containing NPC shows slight decoloration. In contrast, the yellow–brown Na_2S_4/Na_2Se_4 solution becomes clear and transparent after adding the M@NPC composite, indicating the strong adsorption effect of M@NPC to NaPSs/NaPSes. The UV–Vis curves show that the solution with M@NPC exhibits the smallest absorbance without any characteristic bands of Na_2S_4/Na_2Se_4, which further verifies the strong adsorption of M@NPC to NaPSs/NaPSes.

4 Conclusion

In summary, the dual defense system was designed to prevent the shuttle of polysulfides/polyselenides based on MXene in room temperature Na-SeS_2 battery. The as-

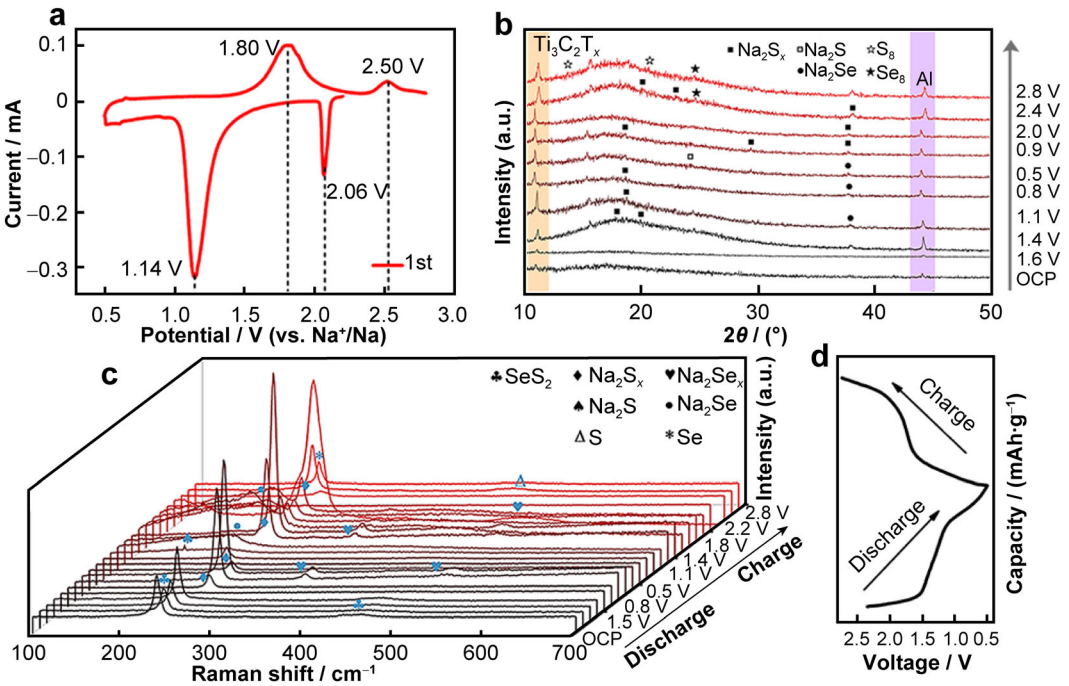

Fig. 5 **a** CV curve at a scan rate of 0.1 mV·s^{-1}; **b** ex-situ XRD patterns, **c** in-situ Raman spectra of SeS_2@M@NPC electrode at different discharge or charge voltages and **d** corresponding discharge/charge profiles

obtained M@NPC composite as SeS_2 host can not only alleviate the volume expansion during charging/discharging but also guarantee rapid ion diffusion, realize the fast kinetics, which acts as the first barrier to prevent the shuttling of polysulfides/polyselenides. In addition, the few-layered $Ti_3C_2T_x$ sheets uniformly coated on the separator act as the second barrier for preventing the shuttle of overflowed polysulfides/polyselenides by physical interception and chemical adsorption. As a result, the cathode-separator dual defense system based on MXene can significantly resist the shuttle of polysulfides/polyselenides, thereby enabling high specific capacity and remarkable rate performance in room temperature Na-SeS_2 battery.

Acknowledgements This study was financially supported by the National Natural Science Foundation of China (Nos. 22179109 and 22005251), Chongqing Natural Science Foundation (No. cstc2020jcyj-zdxmX0010), Central University Fundamental Research Funds (No. SWU-KR22002).

Declarations

Conflict of interests The authors declare that they have no conflict of interest.

References

[1] Zheng ZJ, Ye H, Guo ZP. Recent progress on pristine metal/covalent-organic frameworks and their composites for lithium-sulfur batteries. Energy Environ Sci. 2021;14(4):1835. https://doi.org/10.1039/D0EE03181J.

[2] Qi YR, Li QJ, Wu YK, Bao SJ, Li CM, Chen YM, Wang GX, Xu MW. A Fe_3N/carbon composite electrocatalyst for effective polysulfides regulation in room-temperature Na-S batteries. Nat commun. 2021;12(1):1. https://doi.org/10.1038/s41467-021-26631-y.

[3] Subramanyan K, Divya M, Aravindan V. Dual-carbon Na-ion capacitors: progress and future prospects. J Mater Chem A. 2021;9(15):9431. https://doi.org/10.1039/D0TA12099E.

[4] Syali M, Kumar D, Mishra K, Kanchan DK. Recent advances in electrolytes for room-temperature sodium-sulfur batteries: a review. Energy Storage Mater. 2020;31:352. https://doi.org/10.1016/j.ensm.2020.06.023.

[5] Kumar D, Kanchan DK, Kumar S, Mishra K. Recent trends on tailoring cathodes for room-temperature Na-S batteries. Mater Sci Energy Technol. 2019;2(1):117. https://doi.org/10.1016/j.mset.2018.11.007.

[6] Yang T, Gao W, Guo B, Zhan R, Xu Q, He H, Bao SJ, Li XY, Chen YM, Xu MW. A railway-like network electrode design for room temperature Na-S battery. J Mater Chem A. 2019;7(1):150. https://doi.org/10.1039/C8TA09556F.

[7] Liu Y, Li X, Sun Y, Yang R, Lee Y, Ahn JH. Dual-porosity carbon derived from waste bamboo char for room-temperature sodium-sulfur batteries using carbonate-based electrolyte. Ionics. 2021;27(1):199. https://doi.org/10.1007/s11581-020-03801-4.

[8] Yao Y, Xu R, Chen M, Cheng X, Zeng S, Li D, Zhou X, Wu X, Yu Y. Encapsulation of SeS_2 into nitrogen-doped free-standing carbon nanofiber film enabling long cycle life and high energy density K-SeS_2 battery. ACS Nano. 2019;13(4):4695. https://doi.org/10.1021/acsnano.9b00980.

[9] Abouimrane Ali, Dambournet D, Chapman K W, Chupas P J, Weng W, Amine K. A new class of lithium and sodium rechargeable batteries based on selenium and selenium–sulfur as

a positive electrode. J American Chem Soc. 2012;134(10): 4505–8. https://doi.org/10.1021/ja211766q.
[10] Zhang J, Li Z, Lou XW. A freestanding selenium disulfide cathode based on cobalt disulfide-decorated multichannel carbon fibers with enhanced lithium storage performance. Angew Chem Int Ed. 2017;56(45):14107. https://doi.org/10.1002/anie.201708105.
[11] Li X, Liang J, Luo J, Wang C, Li X, Sun Q, Li R, Zhang L, Yang R, Lu S, Huang H, Sun X. High-performance Li-SeS_x all-solid-state lithium batteries. Adv Mater. 2019;31(17):1808100. https://doi.org/10.1002/adma.201808100.
[12] Li Z, Zhang J, Lu Y, Lou XW. A pyrolyzed polyacrylonitrile/selenium disulfide composite cathode with remarkable lithium and sodium storage performances. Sci Adv. 2018;4(6):1687. https://doi.org/10.1126/sciadv.aat16.
[13] Li X, Wang C, Cao Y, Wang G. Functional MXenes materials: progress of their applications. Chemistry-An Asian Journal. 2018;13(19):2742. https://doi.org/10.1002/asia.201800543.
[14] Aslam M, Niu Y, Xu M. MXenes for non-lithium-ion (Na, K, Ca, Mg, and Al) batteries and supercapacitors. Adv Energy Mater. 2021;11(2):2000681. https://doi.org/10.1002/aenm.202000681.
[15] Dong Y, Zheng S, Qin J, Zhao X, Shi H, Wang X, Chen J, Wu ZS. All-MXene-based integrated electrode constructed by Ti_3C_2 nanoribbon framework host and nanosheet interlayer for high-energy-density Li-S batteries. ACS Nano. 2018;12(3): 2381. https://doi.org/10.1021/acsnano.7b07672.
[16] Cengiz E, Erdol Z, Sakar B, Aslan A, Ata A, Ozturk O, Demir-Cakan R. Investigation of the effect of using Al_2O_3-Nafion barrier on room temperature Na-S batteries. J Phys Chem C. 2017;121(28):15120. https://doi.org/10.1021/acs.jpcc.7b04711.
[17] Yang Q, Yang T, Gao W, Qi Y, Guo B, Zhong W, Jiang J, Xu M. An MXene-based aerogel with cobalt nanoparticles as an efficient sulfur host for room-temperature Na-S batteries. Inorg Chem Front. 2020;7(22):4396. https://doi.org/10.1039/D0QI00939C.
[18] Qiu ZM, Bai Y, Gao YD, Liu CL, Ru Y, Pi YC, Zhang YZ, Luo YS, Pang H. MXenes nanocomposites for energy storage and conversion. Rare Met. 2022;41(4):1101. https://doi.org/10.1007/s12598-021-01876-0.
[19] Chen JZ, Chen MF, Zhou WJ, Xu XW, Liu B, Zhang WQ, Wong CP. Simplified synthesis of fluoride-free $Ti_3C_2T_x$ via electrochemical etching toward high-performance electrochemical capacitors. ACS Nano. 2022;16(2):2461. https://doi.org/10.1021/acsnano.1c09004.
[20] Ma J, Gao L, Li S, Zeng Z, Zhang L, Xie J. Dual play of chitin derived N-doped carbon nanosheets enabling high performance Na-SeS_2 half/full cells. Batteries Supercaps. 2020;3(2):165. https://doi.org/10.1002/batt.201900159.
[21] Sun F, Cheng H, Chen J, Zheng N, Li Y, Shi J. Heteroatomic $SenS_{8-n}$ molecules confined in nitrogen-doped mesoporous carbons as reversible cathode materials for high performance lithium batteries. ACS Nano. 2016;10(9):8289. https://doi.org/10.1021/acsnano.6b02315.
[22] Wang HQ, Zhao YX, Gou L, Wang LY, Wang M, Li Y, Hu SL. Rational construction of densely packed Si/MXene composite microspheres enables favorable sodium storage. Rare Met. 2022; 41(5):1626. https://doi.org/10.1007/s12598-021-01895-x.
[23] Chen JZ, Chen H, Chen MF, Zhou WJ, Tian QH, Wong CP. Nacre-inspired surface-engineered MXene/nanocellulose composite film for high-performance supercapacitors and zinc-ion capacitors. Chem Eng J. 2022;428:131380. https://doi.org/10.1016/j.cej.2021.131380.
[24] Yang T, Qi Y, Zhong W, Tao M, Guo B, Wu Y, Bao SJ, Xu M. A strategy for polysulfides/polyselenides protection based on Co_9S_8@SiO_2/C host in Na-SeS_2 batteries. Adv Funct Mater. 2021;31(2):2001952. https://doi.org/10.1002/adfm.202001952.
[25] Dong W, Chen H, Xia F, Yu W, Song J, Wu S, Deng Z, Hu Z, Tawfique H, Li Y, Wang H, Chen L, Su BL. Selenium clusters in Zn-glutamate MOF derived nitrogen-doped hierarchically radial-structured microporous carbon for advanced rechargeable Na–Se batteries. Journal of Materials Chemistry A. 2018;6(45): 22790–7. https://doi.org/10.1039/C8TA07662F.
[26] Du W, Xu Q, Zhan R, Zhang Y, Luo Y, Xu M. Synthesis of hollow porous carbon microspheres and their application to room-temperature Na-S batteries. Mater Lett. 2018;221:66. https://doi.org/10.1016/j.matlet.2018.03.090.
[27] Yao Yu, Zeng L, Shuhe Hu, Jiang Yu, Yuan B, Yan Yu. Binding $S_{0.6}Se_{0.4}$ in 1D carbon nanofiber with C-S bonding for high-performance flexible Li-S batteries and Na-S batteries. Small. 2017;13(19):1603513. https://doi.org/10.1002/smll.201603513.
[28] Lu Q, Wang X, Cao J, Chen C, Chen K, Zhao Z, Niu Z, Chen J. Freestanding carbon fiber cloth/sulfur composites for flexible room-temperature sodium-sulfur batteries. Energy Storage Mater. 2017;8:77. https://doi.org/10.1016/j.ensm.2017.05.001.
[29] Deng Y, Gong L, Ahmed H, Pan Y, Cheng X, Zhu S, Zhang H. N-doped interconnected carbon aerogels as an efficient SeS_2 host for long life Na-SeS_2 batteries. Nano Res. 2020;13(4): 967–74. https://doi.org/10.1007/s12274-020-2726-8.
[30] Zhang W, Wang H, Zhang N, Liu H, Chen Z, Zhang L, Guo S, Li D, Xu J. One-step in situ preparation of polymeric selenium sulfide composite as a cathode material for enhanced sodium/potassium storage. ACS Appl Mater Interfaces. 2019;11(33): 29807. https://doi.org/10.1021/acsami.9b07540.
[31] Xu GL, Ma T, Sun CJ, Luo C, Cheng L, Ren Y, Heald SM, Wang C, Curtiss L, Wen J, Miller DJ, Li T, Zou X, Petkov V, Chen Z, Amine K. Insight into the capacity fading mechanism of amorphous Se_2S_5 confined in micro/mesoporous carbon matrix in ether-based electrolytes. Nano Lett. 2016;16(4):2663. https://doi.org/10.1021/acs.nanolett.6b00318.
[32] Goldbach A, Iton L, Grimsditch M, Saboungi ML. The formation of Se^{2-}: a new resonance raman feature in the photochemistry of zeolite-encapsulated selenium. J Am Chem Soc. 1996; 118(8):2004. https://doi.org/10.1021/ja9531788.